Wavelength- and ellipticity-dependent photoelectron spectra from multiphoton ionization of atoms

Keyu Guo(郭珂雨)[1], Min Li(黎敏)[1,†], Jintai Liang(梁锦台)[1], Chuanpeng Cao(曹传鹏)[1], Yueming Zhou(周月明)[1], and Peixiang Lu((陆培祥)[1,2]

[1] *School of Physics and Wuhan National Laboratory for Optoelectronics, Huazhong University of Science and Technology, Wuhan* 430074, *China*
[2] *Optics Valley Laboratory, Wuhan* 430074, *China*

(Received 9 September 2022; revised manuscript received 7 October 2022; accepted manuscript online 19 October 2022)

We theoretically study the photoelectron momentum distributions from multiphoton ionization of a model lithium atom over a range of laser wavelengths from 500 nm to 700 nm by numerically solving the time-dependent Schrödinger equation. The photoelectron momentum distributions display many ring-like patterns for the three-photon ionization, which vary dramatically with the change of the laser wavelength. We show that the wavelength-dependent photoelectron energy spectrum can be used to effectively identify the resonant and nonresonant ionization pathways. We also find an abnormal ellipticity dependence of the electron yield for the (2+1) resonance-enhanced ionization via the 4d intermediate state, which is relevant to the two-photon excitation probability from the ground state to the 4d state.

Keywords: multiphoton ionization, ultrafast phenomena, Freeman resonance

PACS: 32.80.–t, 33.80.Rv, 32.80.Rm **DOI:** 10.1088/1674-1056/ac9b36

1. Introduction

Multiphoton ionization (MPI) of atoms and molecules attracted great attention in the past few decades.[1–4] Nowadays, advances in high-power short-pulse laser technologies make it possible to observe many interesting effects in the MPI process, such as laser-intensity dependence of the photoelectron yield,[5] Rabi-flopping effect,[6] and circular dichroism.[7–9] A range of important applications such as laser-induced plasma generation,[10,11] chemical diagnostics,[12,13] molecular structure imaging,[14,15] electron vortices generation,[16] and photoelectron spectroscopy[17] can be implemented through the MPI.

In the MPI process, the photoelectron can be released via either resonant or nonresonant ionization pathways. For the nonresonant ionization, the photoelectron is released directly from the ground state of the atom. On the other hand, when the resonance occurs, the atom is ionized via an intermediate excited state, revealing many fine structures for the low-energy above-threshold ionization peaks in the photoelectron energy spectra. This phenomenon is dubbed Freeman resonance,[18] which can be attributed to ac-Stark shift of the energy level of the excited states of atoms in the laser field. Separation of the resonant and nonresonant ionization signals from the photoelectron spectra is of great significance for investigating many ultrafast processes, such as the inner-shell ionization dynamics,[19] resonant ionization time delay,[20,21] and fine structure threshold effects.[22] Since the shift of the excited state energy level and the ionization threshold depends on the laser intensity by the ac-Stark shift $U_p = I_{laser}/4\omega^2$ with U_p being the ponderomotive energy, ω being the frequency of the laser field, and I_{laser} being the laser intensity, the nonresonant peaks in the photoelectron energy spectra shift towards lower energy as the laser intensity increases while the Freeman resonant peaks do not shift with the laser intensity. Thus by simply scanning the laser intensity, the nonresonant and resonant ionization pathways can be identified and isolated from the intensity-dependent photoelectron energy spectra.[23–25]

Most of previous works about the MPI concentrated on rare gas atoms.[26] For those atoms, the laser field strength corresponding to the MPI regime is far lower than the threshold laser field strength of over-the-barrier ionization (OBI) regime, which is estimated as $E_{OBI} = I_p^2/4$ (Ref. [27]) with I_p being the ionization potential of atoms. For atoms with relatively lower ionization potential, such as Li, Na, K, and Rb atoms, the threshold laser intensity of the OBI regime is about 10^{12} W/cm^2.[28,29] At this laser intensity, the atom is severely ionized and the electron is mainly released during the leading edge of the laser pulse.[30] For the laser intensity below the OBI threshold, U_p becomes very small (smaller than 0.03 eV at a typical laser wavelength of 800 nm).[31] Thus both nonresonant and resonant peaks in the photoelectron energy spectra are nearly unchanged with the laser intensity due to the negligible ac-Stark shift. Moreover, those atoms with relatively low ionization potentials usually have several excited states with similar energy levels complicating the MPI process[32–34] (*i.e.*, the different intermediate states can be reached through a small detuning by absorbing the same number and frequency of photons). Therefore, it is difficult to identify the resonant

†Corresponding author. E-mail: mli@hust.edu.cn

© 2023 Chinese Physical Society and IOP Publishing Ltd

and nonresonant ionization pathways by scanning the intensity of the laser pulse for those atoms.

In this paper, we study the MPI of a model lithium atom in a laser pulse over a wide range of wavelengths by numerically solving the time-dependent Schrödinger equation (TDSE). Previously, a number of consecutive channels switching effects were observed by changing the laser wavelength for rare gas atoms.[35–37] We find that the photoelectron momentum distribution (PMD) reveals many ring-like structures for the three-photon ionization of the model lithium atom which vary significantly with the laser wavelength. We show that several intermediate states can simultaneously be resonant with the laser field in the ionization process. Because the position of the nonresonant and resonant ionization peaks in the photoelectron spectrum is mainly determined by the number of absorbed photons from the intermediate (for resonant ionization) or ground (for nonresonant ionization) states to the continuum, the shift is different with the change of the laser wavelength for the resonant and nonresonant ionization pathways. Thus the wavelength-dependent photoelectron energy spectrum can be used to distinguish those different ionization pathways. Moreover, we also study the MPI for different laser ellipticities. We find an abnormal ellipticity dependence of the electron yield for the $(2+1)$ resonance-enhanced ionization via the 4d intermediate state.

2. Theoretical methods

To obtain the time-dependent wave function of an atom in the laser field, we numerically solve the two-dimensional TDSE with the single-active-electron approximation in length gauge which is expressed as

$$\mathrm{i}\frac{\partial}{\partial t}\Psi(\boldsymbol{r},t)=\Big[H_0+\boldsymbol{r}\cdot\boldsymbol{E}(t)\Big]\Psi(\boldsymbol{r},t), \tag{1}$$

where r is the electron position and $H_0=-(1/2)\nabla^2+V(r)$ is the field-free Hamiltonian. $V(r)=-1/\sqrt{r^2+a^2}$ is a soft-core potential,[38] and the soft-core parameter $a=3$ yields $I_\mathrm{p}=0.1993$ a.u. to match the ionization potential of a model lithium atom. The laser electric field is described as

$$\boldsymbol{E}(t)=f(t)\left(\hat{\boldsymbol{e}}_x\frac{E_0}{\sqrt{1+\varepsilon^2}}\cos\omega t+\hat{\boldsymbol{e}}_y\frac{\varepsilon E_0}{\sqrt{1+\varepsilon^2}}\sin\omega t\right), \tag{2}$$

where E_0 is the field amplitude, ω is the frequency of the laser field, and ε is the pulse ellipticity ($\varepsilon=0$ corresponds to linear polarization). $f(t)$ is a trapezoidal pulse shape which has twenty optical cycles in total with two cycles ramping on and off. In our study, $f(t)$ is given by

$$f(t)=\begin{cases}\sin^2\left(\dfrac{\pi t}{2T}\right), & 0\leqslant t\leqslant 2T,\\ 1, & 2T<t<18T,\\ \sin^2\left(\dfrac{\pi(20T-t)}{2T}\right), & 18T\leqslant t\leqslant 20T,\end{cases} \tag{3}$$

where T is the period of the laser pulse. At the end of the pulse, the wave function is further propagated for an additional ten optical cycles to ensure that all the ionized components move away from the core.[39]

In the numerical simulations, we set the peak intensity of the laser field to be 5×10^{11} W/cm^2, and the laser wavelength varies from 500 nm to 700 nm. The time step is set to be $\Delta t=0.1$ a.u. The cartesian grid space ranges from -600 a.u. to 600 a.u. for both x and y directions with a spatial step of $\Delta x=\Delta y=0.3$ a.u. The TDSE is solved with a split-operator spectral method starting from the ground s state of the atom obtained by the imaginary-time propagation method.[40] It is worth mentioning that after the ground state wave function is obtained, the wave function of the first excited state can be obtained by removing the ground state wave function components at each step of the imaginary-time propagation. Similarly, the wave function of other bound states can also be obtained.

3. Results and discussion

Figure 1 shows the PMDs in a linearly polarized laser field with a peak intensity of $I=5\times10^{11}$ W/cm^2 by solving the TDSE for various laser wavelengths of $\lambda=553$ nm, 573 nm, 593 nm, and 629 nm. The laser pulse is polarized along the p_x direction. In Fig. 1(a), we can see that a ring structure appears at $p=\sqrt{p_x^2+p_y^2}\sim0.3$ a.u. at the wavelength of 553 nm. This ring structure corresponds to three-photon ionization from the ground state, which reveals six lobes within the ring structure. With increasing the wavelength to 573 nm, as shown in Fig. 1(b), we can see two obvious rings in the PMDs, *i.e.*, the weaker one appears at $p\sim0.3$ a.u. while the stronger one appears at about $p\sim0.27$ a.u. Those two rings show different angular distributions, *i.e.*, the ring at $p\sim0.3$ a.u. reveals a six-lobe structure while the ring at $p\sim0.27$ a.u. reveals a two-lobe structure. Moreover, a much weaker ring structure appears at $p\sim0.18$ a.u. This ring also reveals six lobes for the angular distribution. At $\lambda=593$ nm, as shown in Fig. 1(c), three rings appear at $p\sim0.3$ a.u., 0.27 a.u., and 0.24 a.u. Those three rings show a six-lobe, two-lobe, and two-lobe structure for the angular distribution, respectively. In addition, the ring at $p\sim0.18$ a.u. becomes obvious. When the wavelength of the laser field further increases to 629 nm, the ring at $p\sim0.18$ a.u. becomes stronger and it splits into two rings, as shown in Fig. 1(d). Both rings reveal six-lobe structures for the angular distribution. It should be noted that all those ring-like structures in Fig. 1 come from three-photon ionization from the ground state.

In order to reveal the origin of those ring-like structures, we show the angle-integrated photoelectron energy spectrum as a function of the laser wavelength ranging from 500 nm to 700 nm, as shown in Fig. 2. We can see many complex

structures in the wavelength-dependent photoelectron energy spectrum. The ionization is enhanced for different electron energies at several wavelengths, *i.e.*, ~ 1.4 eV at ~ 550 nm, ~ 1.2 eV at ~ 570 nm, ~ 1.3 eV at ~ 590 nm, and near-threshold electrons at ~ 660 nm.

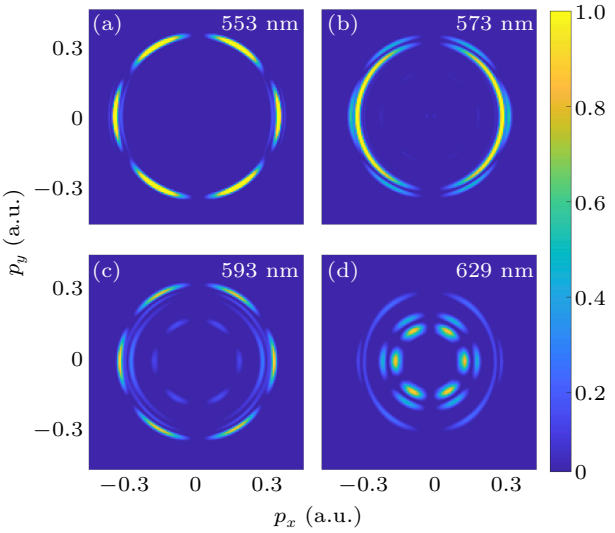


Fig. 1. The PMDs from MPI in a linearly polarized laser field with various laser wavelengths of (a) $\lambda = 553$ nm, (b) $\lambda = 573$ nm, (c) $\lambda = 593$ nm, and (d) $\lambda = 629$ nm.

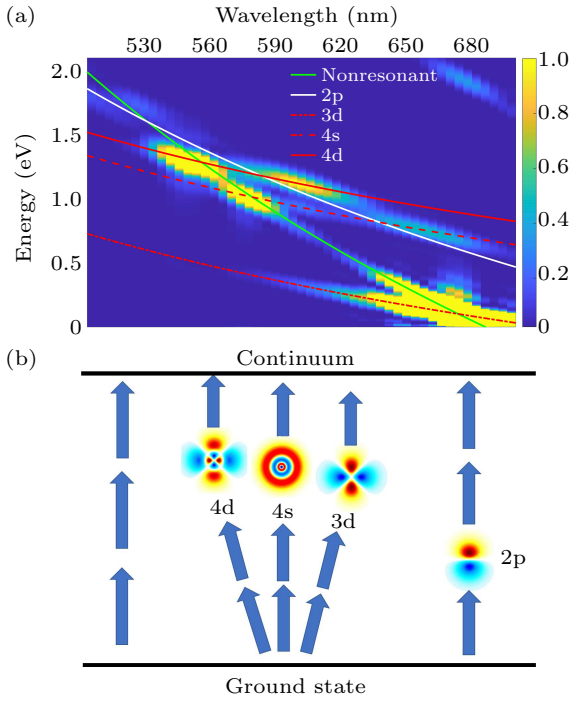


Fig. 2. (a) The wavelength-dependent photoelectron energy spectrum in a linearly polarized laser field. The green solid line represents nonresonant ionization [$n = 3$ in Eq. (4)], the white solid line represents the $(1+2)$ resonant ionization via the 2p intermediate state [$s = 2$ in Eq. (5)], and the red lines represent the $(2+1)$ resonant ionization via the 3d, 4s, and 4d intermediate states [$s = 1$ in Eq. (5)]. (b) Different ionization pathways, *i.e.*, nonresonant ionization (left), $(2+1)$ resonant ionization via the 4d, 4s, and 3d intermediate states (middle), and $(1+2)$ resonant ionization via the 2p intermediate state (right).

To understand those structures in Fig. 2(a), we analyze the dependence of the nonresonant and resonant ionization peaks in the energy spectrum on the laser wavelength. For the nonresonant ionization, the energy of the photoelectron can be described as

$$E_{\text{nonresonant}} = n\omega - I_{\text{p}}, \tag{4}$$

where n is the number of photons that the atoms need to absorb from the ground state. Here we have ignored the effect of the ac-Stark shift because U_{p} is relatively small (U_{p} is smaller than 0.03 eV). For the resonant ionization, the energy of the photoelectron can be described as

$$E_{\text{resonant}} = s\omega + E_i, \tag{5}$$

where s is the number of photons that the atoms need to absorb from the intermediate resonant state, and E_i is the energy level of the intermediate resonant state.

The green solid line in Fig. 2(a) shows the electron energy for the nonresonant ionization as a function of the laser wavelength [$n = 3$ in Eq. (4)]. One can see that the electron energy decreases rapidly with the increase of the wavelength. This nonresonant ionization pathway is illustrated in the left of Fig. 2(b). For the resonant ionization, the energy levels E_i in Eq. (5) of different excited states are obtained by the imaginary-time propagation in TDSE. In Fig. 2, we only show those intermediate states that are relevant to the wavelength-dependent photoelectron energy spectrum by comparing with the TDSE result, *i.e.*, the $(1+2)$ resonance-enhanced ionization via the 2p state (white dashed line) and the $(2+1)$ resonance-enhanced ionization via the 3d, 4s, and 4d states (red dot–dashed, dotted, and solid lines). Those different ionization pathways are shown in Fig. 2(b). One can see that the electron energy of the resonant ionization pathways decreases more slowly than that of the nonresonant ionization pathway with the increase of the wavelength. The slope for the curve of the $(2+1)$ resonant ionization is smaller than that of $(1+2)$ resonant ionization. This can be understood according to Eq. (5). The slope of the dependence of the electron energy on the laser wavelength (or frequency) is determined by the number of photons absorbed from the intermediate state to the continuum. The $(2+1)$ resonant ionization absorbs one photon from the intermediate state to the continuum while the $(1+2)$ resonant ionization need to absorb two photons. Thus the slope of the dependence of the electron energy on the laser wavelength is different. Moreover, we can also see that the ionization is enhanced at those regions when two lines are intersected. Those regions correspond to that the detuning of the resonance approaches zero, leading to the enhancement of the ionization. When the detuning increases, the ionization yield decreases rapidly.

According to those lines in Fig. 2(a), we can identify the origin of different rings in Fig. 1. In Fig. 1(a), the ring structure

comes from the $(2+1)$ resonant ionization via the 4d state. At $\lambda = 573$ nm of Fig. 1(b), the two rings at $p \sim 0.3$ a.u., 0.27 a.u., and 0.18 a.u. come from the $(2+1)$ resonant ionization via the 4d, 4s, and 3d states, respectively. At $\lambda = 593$ nm of Fig. 1(c), the ring at $p \sim 0.3$ a.u. comes from the resonant ionization via the 2p and 4d states. The two rings at $p \sim 0.27$ a.u., and 0.18 a.u. are of the same origin as those in Fig. 1(b). Another ring at $p \sim 0.24$ a.u. comes from the nonresonant ionization. At $\lambda = 629$ nm, as shown in Fig. 2(d), the ring at $p \sim 0.24$ a.u. originates from the $(2+1)$ resonant ionization via the 4s state. The other two rings at $p \sim 0.16$ a.u., and 0.13 a.u. originate from the nonresonant ionization and the $(2+1)$ resonant ionization via the 3d state, respectively. Thus the wavelength-dependent photoelectron energy spectrum allows us to identify the origin of those multiple ring structures in the PMD.

With identifying the ionization pathways from the wavelength-dependent photoelectron energy spectrum, we can further study the ionization dynamics for both resonant and nonresonant ionizations. Next, we mainly focus on the dependence of the photoelectron yield from the resonant ionization pathway on the laser ellipticity. We choose the case of $\lambda = 573$ nm for analysis because the photoelectron yield from resonant ionization via the 4s and 4d states is comparable. The angle-integrated photoelectron energy spectrum for the 4s and 4d states is shown as a function of the ellipticity of the laser field in Fig. 3(a). We can see that the photoelectron yield from resonance-enhanced ionization via the 4s state decreases significantly with the increase of the ellipticity, whereas the yield from resonance-enhanced ionization via the 4d state increases with the increase of the ellipticity. To understand the abnormal ellipticity dependence of the electron yield for the resonant ionization via the 4d state,[41] we show in Fig. 3(b) the normalized population of the 4s and 4d states at the end of the laser pulse from the TDSE result. As we can see, the population of the 4s state decreases while the population of the 4d state increases with the increase of the ellipticity. Thus the ellipticity dependence of the ionization yield comes from the population of the excited states.

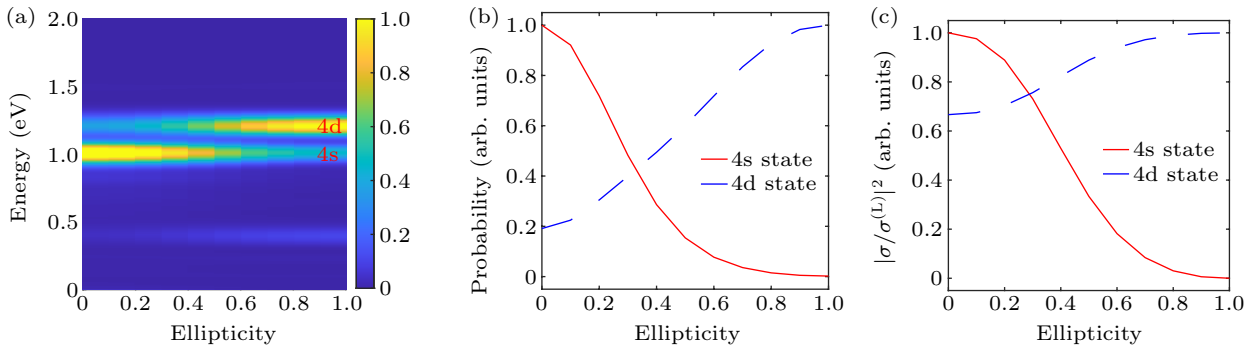


Fig. 3. (a) The ellipticity-dependent photoelectron energy spectrum at the laser wavelength of $\lambda = 573$ nm. 4s and 4d are used to indicate the intermediate states of the resonant ionization for the two most obvious peaks in the energy spectrum. (b) The normalized population at the end of the laser pulse of the 4s state (red line) and the 4d state (blue dotted line) as a function of the laser ellipticity according to the TDSE result. (c) The normalized transition probability from the ground state to the 4s state (red line) and the 4d state (blue dotted line) as a function of the ellipticity according to Eq. (7).

Next we investigate the excitation probability from the ground state and the excited state using the perturbation theory. For both 4s and 4d states, two photons are needed to absorb from the ground state. For such a two-photon absorption process, the transition amplitude from the initial ground state $|g\rangle$ to the excited state $|f\rangle$ with the dipole approximation can be given by[42,43]

$$D = \langle f|(\boldsymbol{\varepsilon}\cdot\boldsymbol{r})M|g\rangle, \tag{6}$$

where $\boldsymbol{\varepsilon}$ is the polarization vector along the polarization direction of the incident radiation field. M is an auxiliary dimensionless operator, which can be written as $M(\boldsymbol{r}) = \psi_1(r)\boldsymbol{\varepsilon}\cdot\boldsymbol{r}$,[42] where $\psi_1(r)$ is the separated function along the radial direction. The ground state and the excited state can be written as $\Phi(\boldsymbol{r}) = R_{nl}(r)\mathrm{Y}_{lm}(\theta,\varphi)$, where $R_{nl}(r)$ is the radial wave function and $\mathrm{Y}_{lm}(\theta,\varphi)$ is the spherical harmonics. n, l, and m are the principal quantum number, angular quantum number, and magnetic quantum number, respectively.

For the 4d state, the two-photon transition can occur in both linearly and circularly polarized laser fields. In the linearly polarized laser field $\boldsymbol{\varepsilon}\cdot\boldsymbol{r} = r\cos\varphi$, we obtain $\left|D_{4d}^{(L)}\right| = \left|\int \mathrm{Y}_{20}^{*}\cos^2\varphi\,\mathrm{Y}_{00}\,\mathrm{d}\varphi\cdot\mathcal{R}_{4d}\right| = (\sqrt{5}/8)\mathcal{R}_{4d}$, and in the circularly polarized laser field $\boldsymbol{\varepsilon}\cdot\boldsymbol{r} = (1/\sqrt{2})r\mathrm{e}^{\mathrm{i}\varphi}$, we obtain $\left|D_{4d}^{(C)}\right| = \left|\int \mathrm{Y}_{22}^{*}\frac{1}{2}\mathrm{e}^{2\mathrm{i}\varphi}\mathrm{Y}_{00}\,\mathrm{d}\varphi\cdot\mathcal{R}_{4d}\right| = (1/8)\sqrt{15/2}\mathcal{R}_{4d}$, where $\mathcal{R}_{4d} = \int \mathrm{d}r R_{42}^{*} r^3\psi_1\,\mathrm{e}^{-r}$ represents the radial part of the transition amplitude, which is independent of the polarization of the laser pulse. For the 4s state, the two-photon transition can occur in linearly polarized laser field while in circularly polarized field the transition is prohibited because of the transition selection rule. We obtain the transition amplitude for the 4s state $\left|D_{4s}^{(L)}\right| = \frac{1}{4}\mathcal{R}_{4s}$, where the radial part of the transition amplitude $\mathcal{R}_{4s} = \int \mathrm{d}r R_{40}^{*} r^3\psi_1\,\mathrm{e}^{-r}$ is also independent of the polarization of the laser pulse. In the circularly polarized laser field, the transition amplitude is zero, *i.e.*, $\left|D_{4s}^{(C)}\right| = 0$.

For the elliptically polarized laser field in Eq. (2), we can treat it as the superposition of a circularly polarized laser field and a linearly polarized laser field, *i.e.*,

$$\boldsymbol{E}(t) = \frac{(1-\varepsilon)E_0}{\sqrt{1+\varepsilon^2}}\hat{e}_x \cos\omega t + \frac{\varepsilon E_0}{\sqrt{1+\varepsilon^2}}(\hat{e}_x \cos\omega t + \hat{e}_y \sin\omega t)$$

by neglecting the pulse envelope. Thus the relative contribution of the linearly and circularly polarized laser fields to the whole intensity of the elliptically polarized laser field can be written as $a_1 = (1-\varepsilon)^2/[2\varepsilon^2 + (1-\varepsilon)^2]$ and $a_2 = 2\varepsilon^2/[2\varepsilon^2 + (1-\varepsilon)^2]$, respectively. The excitation probability σ from the ground state to the excited state is proportional to $|D|^2$ and the intensity of the laser field I,[42] so the ratio of the excitation probability in the ellipticity polarized laser field with arbitrary ellipticity to that in the linearly polarized laser field can be written as, for the 4s and 4d states, respectively,

$$\frac{\sigma_{4\mathrm{d}}}{\sigma_{4\mathrm{d}}^{(\mathrm{L})}} = \frac{a_1\left|D_{4\mathrm{d}}^{(\mathrm{L})}\right|^2 + a_2\left|D_{4\mathrm{d}}^{(\mathrm{C})}\right|^2}{\left|D_{4\mathrm{d}}^{(\mathrm{L})}\right|^2} = \frac{3\varepsilon^2 + (1-\varepsilon)^2}{2\varepsilon^2 + (1-\varepsilon)^2},$$

$$\frac{\sigma_{4\mathrm{s}}}{\sigma_{4\mathrm{s}}^{(\mathrm{L})}} = \frac{a_1\left|D_{4\mathrm{s}}^{(\mathrm{L})}\right|^2 + a_2\left|D_{4\mathrm{s}}^{(\mathrm{C})}\right|^2}{\left|D_{4\mathrm{s}}^{(\mathrm{L})}\right|^2} = \frac{(1-\varepsilon)^2}{2\varepsilon^2 + (1-\varepsilon)^2}. \quad (7)$$

The normalized transition probability as a function of ellipticity is shown in Fig. 3(c) for the 4s and 4d states according to Eq. (7). By comparing the curves in Figs. 3(b) and 3(c), we find that the transition probability reveals the same trend with respect to the ellipticity as the population of the electron yield from the excited state from the TDSE result. Therefore the abnormal ellipticity dependence of the resonant ionization via the 4d intermediate state mainly comes from the effect of the excitation probability from the ground state to the 4d state.

We further study the dependence of the photoelectron angular distribution on the ellipticity for the $(2+1)$ resonant ionization via the 4s and 4d states, as shown in Fig. 4. For the $(2+1)$ resonant ionization via the 4s state, as shown in Fig. 4(a), the photoelectron angular distribution spectrum shows two maxima at $\varepsilon = 0$. The spectrum becomes isotropic with respect to the emission angle at $\varepsilon = 1$. For the 4d state, as shown in Fig. 4(b), the photoelectron angular distribution spectrum shows six maxima at $\varepsilon = 0$ and also becomes isotropic with respect to the emission angle at $\varepsilon = 1$. For relatively small ellipticity value of $\varepsilon < 0.5$, we find that the most probable emission angle for the resonant ionization via the 4s state obviously shifts as a function of the laser ellipticity, while for the 4d state it barely shifts. For relatively large ellipticity value of $\varepsilon > 0.5$, the ionization yield via the 4s state decreases rapidly, while for the 4d state, the six-lobe ring structure keeps unchanged but the intensity of the angular distribution has an unobvious shift. The shifts of the angular distribution may result from the influence of the Coulomb potential. The energy of the photoelectron ionized via the 4s state is lower than that via the 4d state so that the Coulomb potential has a larger influence on the photoelectron ionized via the 4s state. Thus the angular distribution shift for the 4s state is more obvious. More specific explanations need further investigation.

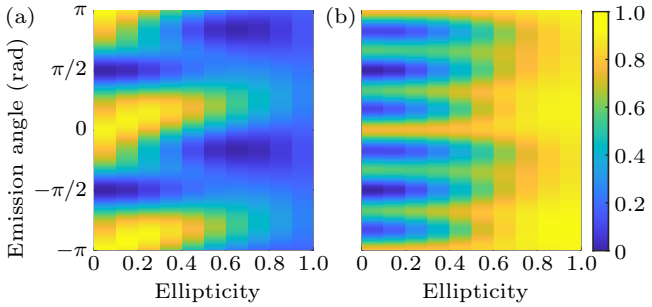


Fig. 4. The photoelectron angular distribution as a function of the laser ellipticity for the $(2+1)$ resonant ionization via the intermediate states of (a) 4s state and (b) 4d state at the laser wavelength of $\lambda = 573$ nm.

4. Conclusion

In conclusion, we have studied the dependence of the photoelectron spectra from three-photon ionization of an atom on the laser wavelength and ellipticity. By continuously changing the wavelength, we show that the wavelength dependence of the electron energy from the nonresonant and resonant pathways reveals different slopes, which is determined by the number of photons absorbed from the resonant (for resonant ionization) or ground (for nonresonant ionization) states to the continuum. Moreover, we find an abnormal ellipticity dependence for the $(2+1)$ resonance-enhanced ionization via the 4d intermediate state, which can be attributed to the effect of the two-photon excitation probability from the ground state to the 4d state. In addition, we find that the angular distribution of the photoelectrons from the resonance-enhanced ionization might also be influenced by the excitation process from the ground state to the intermediate state. Our study enriches the understanding of the MPI process with several resonant states, and might stimulate experimental interests in coherent control of electron dynamics for those atoms or molecules with relatively low ionization potentials.

Acknowledgments

Project supported by National Key Research and Development Program of China (Grant No. 2019YFA0308300) and the National Natural Science Foundation of China (Grant Nos. 12021004 and 61475055).

References

[1] Rhodes C K 1985 *Science* **229** 1345
[2] Mevel E, Breger P, Trainham R, Petite G, Agostini P, Migus A, Chambaret J P and Antonetti A 1993 *Phys. Rev. Lett.* **70** 406

[3] Zhang L, Miao Z, Zheng W, Zhong X and Wu C 2019 *Chem. Phys.* **523** 52

[4] Benda J and Mašín Z 2021 *Sci. Rep.* **11** 11686

[5] Potvliege R M, Meşe E and Vučić S 2010 *Phys. Rev. A* **81** 053402

[6] Tumakov D A, Telnov D A, Plunien G and Shabaev V M 2019 *Phys. Rev. A* **100** 023407

[7] Ilchen M, Douguet N, Mazza T, Rafipoor A J, Callegari C, Finetti P, Plekan O, Prince K C, Demidovich A, Grazioli C, Avaldi L, Bolognesi P, Coreno M, Di Fraia M, Devetta M, Ovcharenko Y, Düsterer S, Ueda K, Bartschat K, Grum-Grzhimailo A N, Bozhevolnov A V, Kazansky A K, Kabachnik N M and Meyer M 2017 *Phys. Rev. Lett.* **118** 013002

[8] De Silva A H, Atri-Schuller D, Dubey S, Acharya B P, Romans K L, Foster K, Russ O, Compton K, Rischbieter C, Douguet N, Bartschat K and Fischer D 2021 *Phys. Rev. Lett.* **126** 023201

[9] De Silva A H, Moon T, Romans K L, Acharya B P, Dubey S, Foster K, Russ O, Rischbieter C, Douguet N, Bartschat K and Fischer D 2021 *Phys. Rev. A* **103** 053125

[10] Buschlinger R, Nolte S and Peschel U 2014 *Phys. Rev. B* **89** 184306

[11] Sharma A, Slipchenko M N, Shneider M N, Wang X, Rahman K A and Shashurin A 2018 *Sci. Rep.* **8** 2874

[12] Ryszka M, Pandey R, Rizk C, Tabet J, Barc B, Dampc M, Mason N J and Eden S 2016 *Int. J. Mass Spectrom.* **396** 48

[13] Sharma A, Braun E L, Patel A R, Arafat Rahman K, Slipchenko M N, Shneider M N and Shashurin A 2020 *J. Appl. Phys.* **128** 141301

[14] Berrah N, Sanchez-Gonzalez A, Jurek Z, Obaid R, Xiong H, Squibb R J, Osipov T, Lutman A, Fang L, Barillot T, Bozek J D, Cryan J, Wolf T J, Rolles D, Coffee R, Schnorr K, Augustin S, Fukuzawa H, Motomura K, Niebuhr N, Frasinski L J, Feifel R, Schulz C P, Toyota K, Son S K, Ueda K, Pfeifer T, Marangos J P and Santra R 2019 *Nat. Phys.* **15** 1279

[15] Garcia Ruiz R F, Vernon A R, Binnersley C L, Sahoo B K, Bissell M, Billowes J, Cocolios T E, Gins W, De Groote R P, Flanagan K T, Koszorus A, Lynch K M, Neyens G, Ricketts C M, Wendt K D, Wilkins S G and Yang X F 2018 *Phys. Rev. X* **8** 041005

[16] Pengel D, Kerbstadt S, Johannmeyer D, Englert L, Bayer T and Wollenhaupt M 2017 *Phys. Rev. Lett.* **118** 053003

[17] Champenois E G, Shivaram N H, Wright T W, Yang C S, Belkacem A and Cryan J P 2016 *J. Chem. Phys.* **144** 014303

[18] Freeman R R, Bucksbaum P H, Milchberg H, Darack S, Schumacher D and Geusic M E 1987 *Phys. Rev. Lett.* **59** 1092

[19] Ho P J, Bostedt C, Schorb S and Young L 2014 *Phys. Rev. Lett.* **113** 253001

[20] Su J, Ni H, Jaroń-Becker A and Becker A 2014 *Phys. Rev. Lett.* **113** 263002

[21] Ke Q H, Zhou Y M, Liao Y J, Liang J T, Zhao Y, Tan J, Li M and Lu P X 2021 *Front. Phys.* **16** 52503

[22] Pradhan A K, Chen G X, Nahar S N and Zhang H L 2001 *Phys. Rev. Lett.* **87** 183201

[23] Li M, Zhang P, Luo S, Zhou Y, Zhang Q, Lan P and Lu P 2015 *Phys. Rev. A* **92** 063404

[24] Shao Y, Li M, Liu M M, Sun X, Xie X, Wang P, Deng Y, Wu C, Gong Q and Liu Y 2015 *Phys. Rev. A* **92** 013415

[25] Song L L, Sun Y N, Wang Y H, Wang X C, He L H, Luo S Z, Hu W H, Tong Q N, Ding D J and Liu F C 2019 *Chin. Phys. B* **28** 063201

[26] Chen Z, Morishita T, Le A T, Wickenhauser M, Tong X M and Lin C D 2006 *Phys. Rev. A* **74** 053405

[27] Augst S, Strickland D, Meyerhofer D D, Chin S L and Eberly J H 1989 *Phys. Rev. Lett.* **63** 2212

[28] Yuan J, Ma Y, Li R, Ma H, Zhang Y, Ye D, Shen Z, Yan T, Wang X, Weidemüller M and Jiang Y 2020 *Chin. Phys. Lett.* **37** 053201

[29] Morishita T and Lin C D 2013 *Phys. Rev. A* **87** 063405

[30] Potvliege R M and Vuić S 2006 *Phys. Scr.* **74** C55

[31] Schuricke M, Zhu G, Steinmann J, Simeonidis K, Ivanov I, Kheifets A, Grum-Grzhimailo A N, Bartschat K, Dorn A and Ullrich J 2011 *Phys. Rev. A* **83** 023413

[32] Jheng S D and Jiang T F 2013 *J. Phys. B: At. Mol. Opt. Phys.* **46** 115601

[33] Hart N A, Strohaber J, Kolomenskii A A, Paulus G G, Bauer D and Schuessler H A 2016 *Phys. Rev. A* **93** 063426

[34] Wessels P, Ruff B, Kroker T, Kazansky A K, Kabachnik N M, Sengstock K, Drescher M and Simonet J 2018 *Commun. Phys.* **1** 32

[35] Marchenko T, Muller H G, Schafer K J and Vrakking M J 2010 *J. Phys. B: At. Mol. Opt. Phys.* **43** 095601

[36] Marchenko T, Muller H G, Schafer K J and Vrakking M J 2010 *J. Phys. B: At. Mol. Opt. Phys.* **43** 185001

[37] Kaminski P, Wiehle R, Renard V, Kazmierczak A, Lavorel B, Faucher O and Witzel B 2004 *Phys. Rev. A* **70** 053413

[38] Barth I and Lein M 2014 *J. Phys. B: At. Mol. Opt. Phys.* **47** 204016

[39] He P L, Takemoto N and He F 2015 *Phys. Rev. A* **91** 063413

[40] Kosloff R and Kosloff D 1986 *J. Comput. Phys.* **63** 363

[41] Delibašić H and Petrović V 2019 *Chin. Phys. B* **28** 083201

[42] Jayadevan A P and Thayyullathil R B 2001 *J. Phys. B: At. Mol. Opt. Phys.* **34** 699

[43] Radhakrishnan R and Thayyullathil R B 2004 *Phys. Rev. A* **69** 033407